Mechanistic Insights on Coverage-Dependent Selectivity Limitations in Vinyl Acetate Synthesis

Gregory L. Novotny[a] and Prashant Deshlahra*[a]

[a]Department of Chemical and Biological Engineering, Tufts University, Medford, Massachusetts 02155, USA

*Email: prashant.deshlahra@tufts.edu

Abstract

Developing improved catalysts for sustainable chemical processes often involves understanding atomistic origins of catalytic activity, selectivity, and stability. Using density functional theory and steady-state kinetic analyses, we probe the elementary steps that form decomposition products that limit selectivity in vinyl acetate (VA) synthesis on Pd surfaces covered with acetate species. Acetate formation and coupling with ethylene control the VA formation catalytic cycle and steady-state coverage, but acetate and ethylene can separately decompose to form CO_2. Both decompositions involve initial C-H activations at acetate vacancies, followed by additional C-H activations and eventual C-O formations and C-C cleavages involving reactions with molecular oxygen. Acetate decomposition paths with non-oxidative kinetically-relevant steps exhibit similar free energy barriers to oxidative paths. In contrast, the non-oxidative ethylene path involving an ethylidyne intermediate exhibits a much lower barrier than paths with oxidative kinetically-relevant steps. Ethylene decomposition is very facile at low coverages but is more coverage-sensitive, leading to similar decomposition and VA formation barriers at coverages accessible at steady state, which is consistent with moderate VA selectivity in measurements and ethylene vs. acetate decomposition contributions assessed from regressed kinetic parameters. These insights provide a detailed framework for describing VA synthesis rates and selectivity on metallic catalyst surfaces.

Introduction

Vinyl acetate (VA) monomer is a valuable building block for producing widely used coatings and adhesives. Its increasing demand and the use of ethylene-VA copolymer as an encapsulant for solar cells have rejuvenated interest in improving the efficiency and sustainability of the VA production process. Industrial VA synthesis is carried out using gas-phase oxidative coupling of ethylene

(C_2H_4) and acetic acid (CH_3COOH) on an alkali-promoted Pd-rich PdAu bimetallic catalyst.[1-4] The mechanisms and composition effects for this reaction have been studied over Pd, PdAu and a few other Pd-based bimetallic catalysts.[5-8] Analyses based on surface science and density functional theory (DFT) have shown that VA formation involves surfaces predominantly covered with acetate species (CH_3COO*; * indicates a surface site), which promote selective acetate-ethylene coupling to form VA over undesired oxidative decomposition products (CO, CO_2). The high acetate coverage conditions can also extensively restructure catalyst nanoparticles and leach Pd from metallic surfaces to form molecular Pd-diacetate complexes that can lead to catalyst deactivation,[4,9-15] though VA synthesis can also be mediated homogeneously by these diacetate complexes.[16] Selectivity and stability are important considerations for efficient processes, and both are enhanced significantly by alloying with Au.[1,6,13,17-22] Alkali acetate promoters enhance PdAu restructuring but decrease the formation of inactive Pd-diacetate trimers, which increases activity, selectivity, and stability.[14-15,23-24] Despite these advances in understanding the functioning of Pd-based catalysts, current catalysts involve expensive precious metals, have a limited lifetime (~1–2 yrs), and require alkali promoter cofeeding. A more detailed understanding of reactive intermediates and transition states that control the formation of VA and undesired products, and of the dependence of their energies on surface properties, can help identify more efficient catalysts. The high-coverage VA synthesis conditions, however, make it challenging to develop such insights through molecular simulation.

Previous ultrahigh vacuum surface science and DFT studies probing titrations of CH_3COO* on the Pd(111) surface[2,7,25-28] revealed that VA synthesis involves a Samanos-type mechanism,[29] with C–O coupling between CH_3COO* and C_2H_4* to form an acetoxyethyl intermediate, followed by C–H activation to form VA (Scheme 1). The insights on VA formation steps were recently expanded by investigating the full catalytic cycle, in which both formation and consumption of CH_3COO* at steady state were considered by combining kinetic measurements on large Pd/SiO_2 nanoparticles (~10 nm) at atmospheric pressure and DFT calculations on Pd(111).[30] These analyses suggest that VA synthesis involves a catalytic cycle analogous to the Mars-van Krevelen (MvK) cycle on metal oxides, with kinetic coupling between steps that form and consume CH_3COO* (in contrast to lattice oxygens in MvK). The DFT calculations showed that rate constants for CH_3COO* formation and consumption change by many orders of magnitude as coverage changes, and that accessible steady-state coverages span a narrow range where both have

similar magnitudes, which illustrates the importance of modeling this reaction at multiple coverages to capture trends in reaction barriers. Monometallic Pd surfaces, however, are only moderately selective to VA, and the elementary steps that limit selectivity by forming CO and CO_2 (Scheme 1) under VA synthesis conditions are not well-understood.

Scheme 1. Desired and undesired products and reactive intermediates in oxidative conversion of ethylene and acetic acid on Pd(111). TS4S is shown in the SI (Fig. S2).

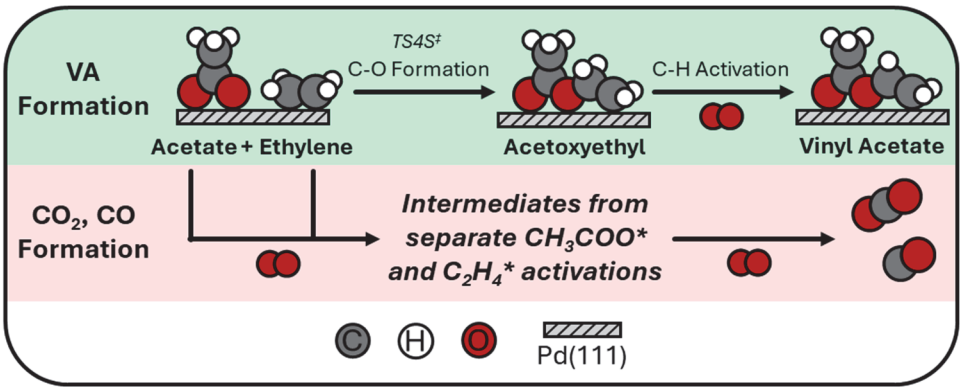

Selectivity to VA has primarily been studied empirically via effects of reactant composition on measured selectivity at some reaction conditions,[31] though some more detailed studies also use isotopic tracing with deuterium[32] or ^{13}C.[33-34] These investigations showed that both CH_3COOH and C_2H_4 are converted to decomposition products under VA synthesis conditions. The relative contributions of CH_3COOH and C_2H_4 depend on reaction conditions, but the specific mechanisms of their conversion remain unclear. To our knowledge, the DFT analyses for VA selectivity were limited to secondary decompositions of VA or the acetoxyethyl intermediates on Pd(100).[28,32] Recently, the Árnadóttir group studied low-coverage CH_3COOH decomposition with and without solvent H_2O, identifying most-favored paths involving decarboxylation and decarbonylation from a key CH_2COO* species in the absence of O_2 or O* species.[35-36] Some proposed mechanisms for CH_3COOH oxidation in atmospheric chemistry involve glyoxylic acid as a key intermediate.[37] For C_2H_4, activated combustion (direct abstraction of H from C_2H_4* by O*) was proposed based on kinetic analysis on Pd/SiO_2 and temperature-programmed reaction spectroscopy on Pd(100);[31,38] however, the high acetate coverages present at steady state strongly inhibit O_2* decomposition, making this route unlikely.[30] Alternatively, ethylidyne (CCH_3*), which is known to be formed by rapid dehydrogenation of C_2H_4* on the (111) facet of platinum-

group metals,[28,39-41] can be a key intermediate for C_2H_4 oxidation. High coverage has also been suggested to inhibit this dehydrogenation,[25] making it important to study these steps at coverages relevant for VA synthesis.

This work uses DFT calculations and steady-state experimental selectivity measurements to evaluate paths for CH_3COO* and C_2H_4* decomposition at coverage ranges relevant to VA synthesis to identify which routes are favored at these conditions, whether the kinetically relevant steps are oxidative or non-oxidative in nature, how their energetics compare to VA formation steps, and how their contributions change with surface coverage. The measured selectivity was unaffected by accumulated products in tests with changing residence times, suggesting that selectivity limitations arise from direct conversions of CH_3COO* and C_2H_4* instead of secondary reactions of VA. For CH_3COO*, facile non-oxidative C–H activation leads to kinetically relevant transfer of Pd-bound H* species to adjacent CH_3COO* species or to O_2*. For C_2H_4*, initial non-oxidative C–H activation is rate-limiting. These steps lead to CH_2COO* and CCH_3* species that are converted to CO_2 in rapid, kinetically irrelevant oxidative steps. For CH_3COO*, oxidative and non-oxidative steps are competitive, while for C_2H_4*, only the non-oxidative step is favorable. Increasing coverage destabilizes C_2H_4* activations more strongly than CH_3COO* activations, but at steady-state coverage both have activation barriers similar to C–O coupling for VA formation. The DFT results informed kinetic equations that were regressed to measured selectivity data over a broad range of reaction conditions. The regression results suggest non-oxidative and oxidative initial CH_3COO* activations and only non-oxidative C_2H_4* activation are relevant for describing measured selectivity trends, which agrees well with the DFT results. These findings lead to a full steady-state mechanistic framework that harmonizes experiment and theory to describe VA formation rates and selectivities on Pd catalysts and identifies most-favored and less-favored paths that may be relevant for other catalysts.

Results and Discussion

Residence Time Test for Secondary Reactions

VA synthesis rate and selectivity were measured in a fixed bed flow reactor on a 1 wt.% Pd/SiO_2 catalyst prepared by incipient wetness impregnation as described elsewhere.[30] We first examined how the selectivity to VA and undesired products CO and CO_2 (with trace amounts of acetaldehyde) change with varying contact times between the catalyst and the reactants, achieved

by varying flow rates with a constant feed composition of reactants, as shown in Fig. 1. As the flow rate decreases from 100 cm^3min^{-1} to 20 cm^3min^{-1}, the conversion increases, resulting in an increase in accumulated VA partial pressure from 0.06 to 0.18 kPa. Over this conversion range the product selectivity remains constant, suggesting that the accumulated primary VA product at higher conversion does not undergo significant secondary reactions. Therefore, the undesired CO and CO_2 products originate directly from CH_3COOH and C_2H_4 as parallel products to VA (Scheme 1). We next perform DFT calculations to determine the likely mechanism for these conversions before returning to changes in measured VA selectivities for different reactant pressures and kinetic equations that accurately describe such changes.

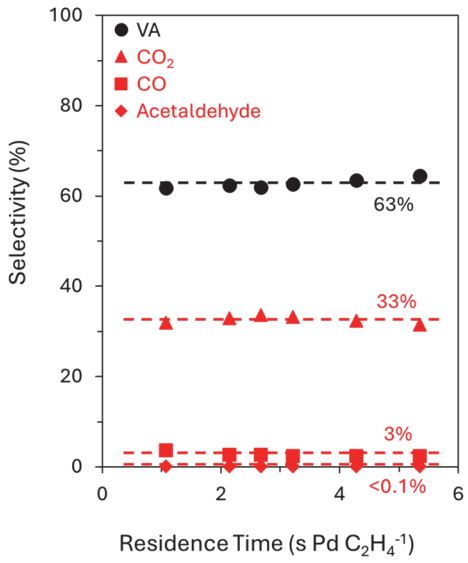

Figure 1. Selectivity to VA, CO_2, and CO, based on number of C atoms in products, as a function of C_2H_4 residence time. Measurements collected on a 1 wt.% Pd/SiO_2 catalyst at 433 K, 40 kPa C_2H_4, 12 kPa CH_3COOH, and 5 kPa O_2 with C_2H_4 conversion <1%, CH_3COOH conversion <4%, and O_2 conversion <14%. Dashed lines show trends.

Surface Models for High Acetate Coverages

To represent the acetate-covered surfaces relevant for VA synthesis, DFT calculations were performed on 3-layer Pd slabs using p(4×4) supercells with 7/16, 6/16, and 5/16 coverages, where *x*/16 indicates *x* CH_3COO* per 16 surface Pd atoms, as shown in Fig. 2. Potentially kinetically relevant transition states were then recalculated with 4-layer Pd slabs and tighter convergence

parameters to enhance the accuracy of reported barriers, as described in the computational methodology (Supporting Information, SI, Section S1) and tabulated in the SI (Table S5). CH_3COO* species adsorb in bidentate configurations on metal surfaces, leading to a maximum coverage of 8/16 with two tightly packed rows (Fig. 2a, highlight shows a complete row). Lower coverages are obtained by sequentially removing CH_3COO* and moving remaining species to find the lowest-energy configurations. Some *ab initio* molecular dynamics were also performed at 5/16 coverage to confirm that no configurations more stable than those obtained from manual perturbations are available.[30] A CH_3COO* vacancy in one of the rows created for 7/16 coverage becomes more stable when one CH_3COO* from the full row moves in between the two rows to more evenly distribute the repulsive interactions (V1, Fig. 2b). For 6/16 and 5/16 coverages, the ordered arrangements with one or two vacancies in each row and no CH_3COO* species crossing the rows are the most stable (Fig. 2c-d). Barriers for CH_3COO* shifting are below 10 kJ mol^{-1}, suggesting that CH_3COO* species can rapidly reorient to attain lower-energy configurations when additional adsorbates are present.[30] Therefore, the structures in Fig. 2 were taken as reference states for each given coverage, but energies of critical intermediates and transition states were calculated with multiple acetate configurations, and the most stable structures are reported.

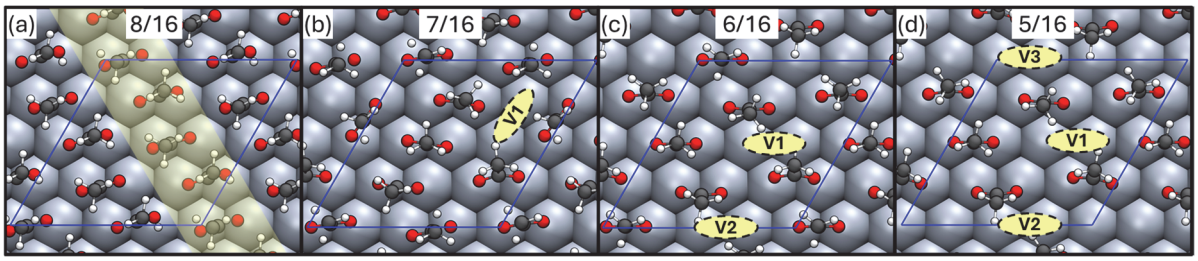

Figure 2. Optimized CH_3COO* adsorption configurations for a Pd(111) surface with (a) 8/16, (b) 7/16, (c) 6/16, and (d) 5/16 coverages, where x/16 represents x CH_3COO* per 16 surface Pd atoms. Blue parallelograms show unit cell boundaries. V2 and V3 are optimal acetate vacancy positions defined relative to the arbitrary position of V1. The highlight strip in (a) shows a complete row of acetates without a vacancy.

Our previous work has shown that VA formation occurs via kinetic coupling between steps that form new CH_3COO* at vacancies in highly covered surfaces and steps that consume the acetate species by coupling with C_2H_4 to form VA (details in the SI, Figs. S1 and S2).[30] The

CH_3COO^* formation steps exhibit much lower barriers than the consumption steps at 5/16 and lower coverages, suggesting that more acetates can readily form at these low coverages but cannot be removed at comparable rates. However, barriers for formation steps increase more sensitively with coverage and become similar to consumption steps as coverage approaches 6/16, suggesting that the steady state surface is near this higher coverage. Here, we probe coverage dependencies for CH_3COO^* and $C_2H_4^*$ decomposition steps. We first describe in detail possible decomposition paths at 6/16 coverage before examining the kinetically relevant transition states along the most favorable paths at lower and higher coverages.

Decomposition of Acetate Species at 6/16 Coverage

Scheme 2. Possible oxidative (orange arrows) and non-oxidative (black arrows) steps involved in the conversion of acetate-derived species to undesired products. Bold arrows show the most favored paths. Relevant transition states labeled with double-dagger symbols are found in Fig. 3 (TS1–TS4) or the SI (Figs. S4 and S5).

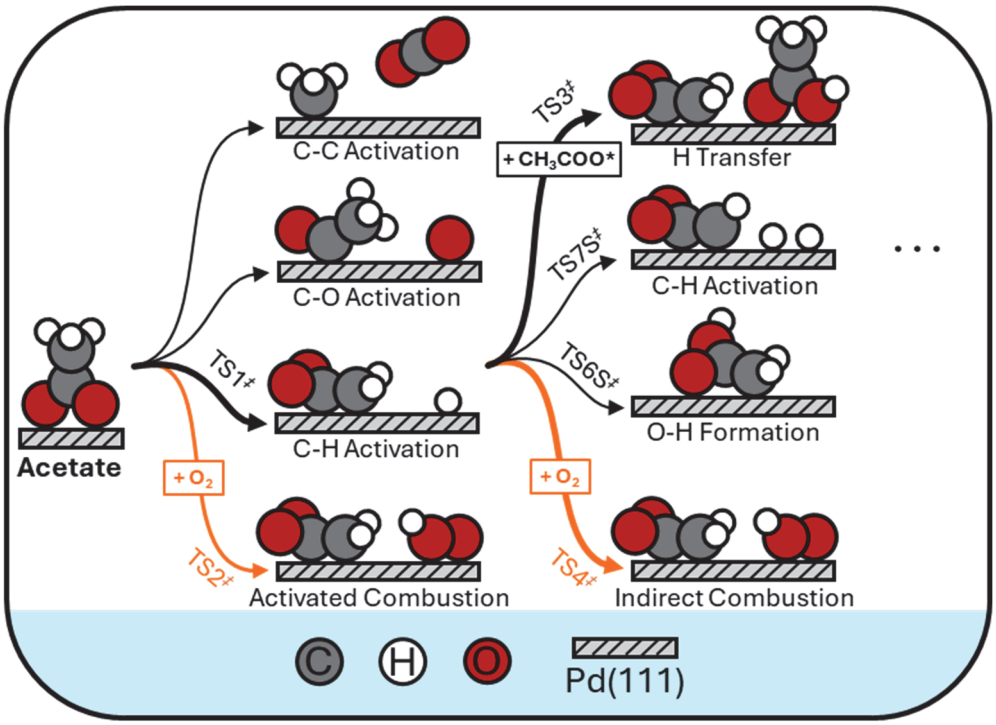

Scheme 2 shows possible initial steps in non-oxidative and oxidative decomposition routes for CH_3COO^* species. The non-oxidative route can involve C–C, C–O or C–H cleavage steps, releasing a CH_3^*, O* or H* species on the Pd atoms at a vicinal CH_3COO^* vacancy site at 6/16

coverage (V1, Fig. 2c). Previous work at low coverage has shown that C–C and C–O activations of CH_3COO* on Pd(111) involve transition states with much higher energy than C–H activations.[35-36] We compared the energies of the three types of transition states at 6/16 coverage as shown in the SI (Fig. S4, transition state electronic energies $\Delta E^{\ddagger}_{\mathrm{C-H}}$=77 kJ mol^{-1}, $\Delta E^{\ddagger}_{C-O}$=156 kJ mol^{-1}, $\Delta E^{\ddagger}_{\mathrm{C-C}}$=173 kJ mol^{-1}), which confirms that C–H activation is strongly favored over C–C and C–O activations. In oxidative and acetate-covered VA synthesis conditions, this C–H activation can involve H transfer to vicinal O_2* or CH_3COO* as well (Scheme 2). Fig. 3 shows electronic energies, free energies at 433 K (calculated from enthalpy and entropy contributions using ideal gas statistical mechanics, as described in the SI, Section S1), and structures for intermediates and transition states involved in the most favorable oxidative and non-oxidative paths for acetate conversion to CO_2, referenced to 6/16 acetate coverage and gas-phase reactants (10 kPa CH_3COOH, C_2H_4, O_2). Corresponding enthalpy and entropy contributions are shown in the SI (Table S1). Other possible but less favorable branches are shown in the SI for comparison (Figs. S5 and S6).

A bidentate acetate (η^2–CH_3COO*) first converts to a monodentate form (η^1–CH_3COO*; Fig. 3a, ΔE=11 kJ mol^{-1}; Fig. 3b, ΔG=-4 kJ mol^{-1}). The conversion of this η^1–CH_3COO* species to CH_2COO* and H* is mediated by a non-oxidative C–H activation transition state (TS1; Fig. 3a, $\Delta E^{\ddagger}$=77 kJ mol^{-1}; Fig. 3b, $\Delta G^{\ddagger}$=66 kJ mol^{-1}) that transfers an H atom to the Pd surface and leaves the CH_2 group bound to an adjacent Pd atom. An alternative transition state involving a C–H activation directly from η^2–CH_3COO* was found to be much less stable (SI, Fig. S7, $\Delta E^{\ddagger}$=113 vs. 77 kJ mol^{-1} for η^2– vs. η^1–CH_3COO*). These results contrast past studies that report C–H activation from η^2–CH_3COO*.[35-36] To probe this apparent discrepancy we calculated both types of transition states at 1/16 coverage and found that C–H activation from η^2–CH_3COO* is indeed more favorable at low coverages (SI, Fig. S7; $\Delta E^{\ddagger}$=102 vs. 139 kJ mol^{-1} for η^2– vs. η^1–CH_3COO*). Thus, our results are consistent with previous low-coverage work but reveal new lower-energy paths enabled by high coverage, where adsorbate-adsorbate repulsion causes weaker binding of the acetate O-atoms, enabling re-orientation to an η^1–CH_3COO* configuration suitable for more facile H transfer to the surface.

At 6/16 coverage, an O_2 molecule can also adsorb at an acetate vacancy vicinal to η^1–CH_3COO* and abstract an H atom from the CH_3 group via a transition state that exhibits a much lower electronic energy than the non-oxidative C–H activation due to strong O_2-surface

interaction; however, the compensating entropy loss from O_2 adsorption leads to a slightly higher free energy (orange dotted line in Fig. 3; TS2, $\Delta E^{\ddagger}$=-5, $\Delta G^{\ddagger}$=78 kJ mol^{-1}). Thus, for the initial C–H activation, the non-oxidative route is favored (by 12 kJ mol^{-1}), but subsequent steps must also be considered to identify the highest energy step in each route, which we discuss next.

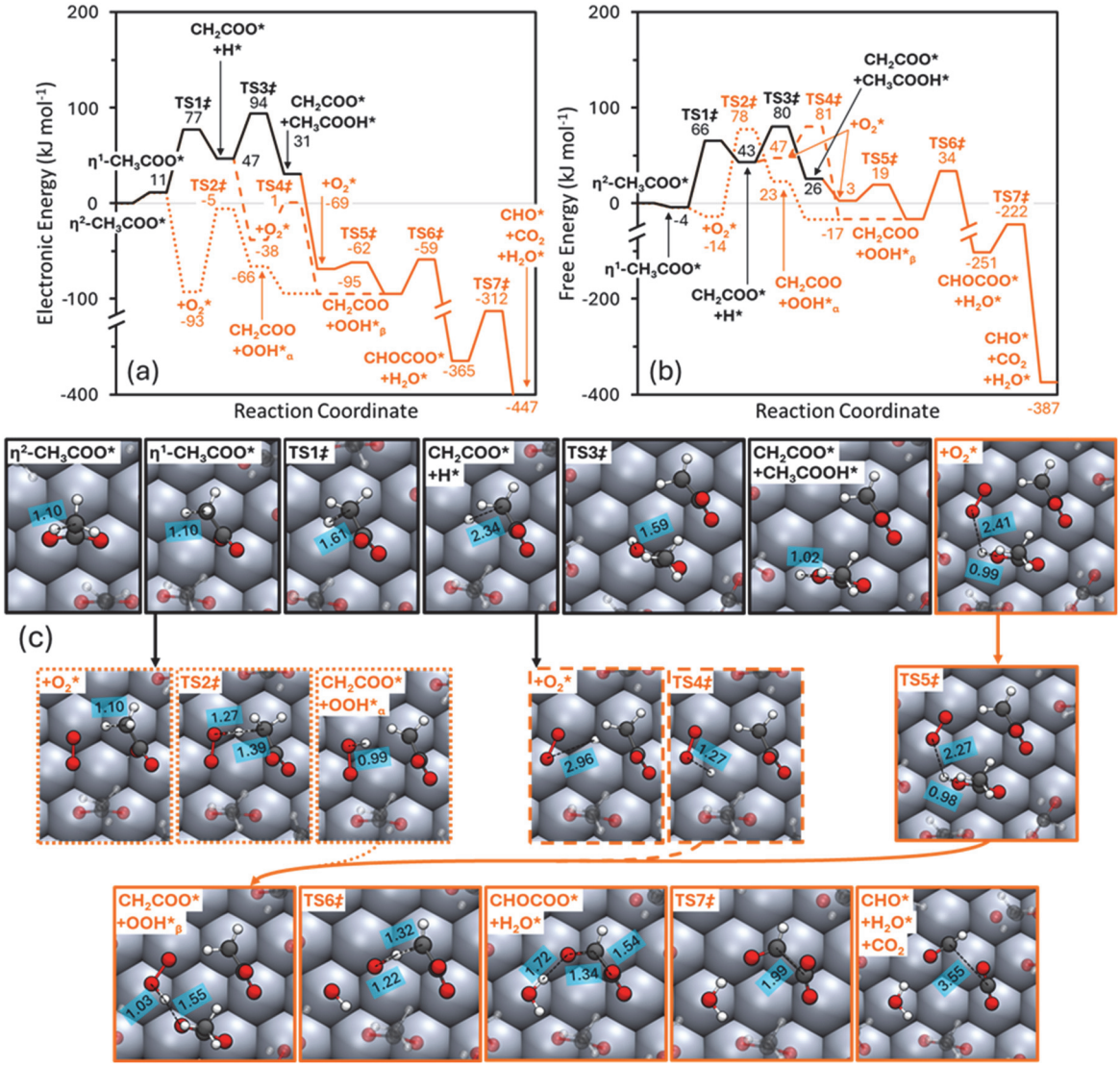

Figure 3. PBE-D3BJ-derived (a) electronic energies, (b) Gibbs free energies at 433K and 10 kPa gaseous reactants, and (c) structures for intermediates and transition states involved in non-oxidative (black) and oxidative (orange) decomposition of CH_3COO* at 6/16 coverage. Note the axis breaks in (a) and (b). Bond distances are in Å. Spectator acetates are shown as transparent structures. Corresponding energy, enthalpy, entropy, and free energy are tabulated in the SI (Table S1).

After the initial non-oxidative C–H activation, an O_2 molecule can adsorb at an acetate vacancy vicinal to the Pd-bound H* species and abstract the H* from the surface to form an OOH* species via a transition state nearly identical in energy to that of O_2*-assisted C–H activation of η^1–CH_3COO* (orange dashed line in Fig. 3; TS4, $\Delta E^{\ddagger}$=1, $\Delta G^{\ddagger}$=81 kJ mol^{-1}). Alternatively, the Pd-bound H* species can be transferred to a vicinal η^2–CH_3COO* species via an O–H formation transition state that forms CH_3COOH* (solid black line in Fig. 3; TS3, $\Delta E^{\ddagger}$=94, $\Delta G^{\ddagger}$=80 kJ mol^{-1}). A transition state for the direct transfer of an H atom from the CH_3 group of the η^1–CH_3COO* to a vicinal η^2–CH_3COO*, bypassing the intermediate transfer of H to the Pd surface, was found to be much less stable than the transition state for H transfer to Pd (SI, Fig. S5, TS5S, $\Delta E^{\ddagger}$=135, $\Delta G^{\ddagger}$=123 kJ mol^{-1}). After CH_3COOH* formation, O_2 adsorption is exergonic (solid orange line in Fig. 3), and CH_3COOH* can rapidly transfer H to the vicinal O_2* to form OOH* (Fig. 3; TS5, $\Delta E^{\ddagger}$= -62, $\Delta G^{\ddagger}$=19 kJ mol^{-1}).

Alternative transfer of H* onto CH_2COO* to form CH_2COOH*, or continued C–H activation of CH_2COO* to form additional H* species, are unfavorable, as shown in the SI (Fig. S5). Desorption of CH_3COOH* was also considered (Fig. S6); however, both non-oxidative ($\Delta G^{\ddagger}$=100 kJ mol^{-1}) and oxidative ($\Delta G^{\ddagger}$=105 kJ mol^{-1}) decomposition of CH_2COO* after this desorption have much higher barriers than the path shown in Fig. 3. Therefore, the most favorable paths for CH_3COO* decomposition all involve the formation of CH_2COO* and OOH*.

The reactive OOH* species can abstract an additional H atom from the vicinal CH_2COO*, forming H_2O and CHOCOO*, or glyoxylate, a proposed intermediate in the atmospheric oxidation of acetic acid.[37] To form this glyoxylate species, the O atom in OOH* separates from the OH group and abstracts an H atom from CH_2COO*, with subsequent facile H transfer between two resulting OH groups and concomitant O–CH formation. Fig. S8 in the SI shows a minimum energy path derived from a nudged elastic band calculation, demonstrating that the H transfer from CH_2 to O is the highest energy point along the path while the subsequent steps are essentially barrierless due to the highly exothermic nature of the transformation involved. The C–H activation transition state for this highest-energy point is shown as TS6 in Fig. 3 ($\Delta E^{\ddagger}$=-59, $\Delta G^{\ddagger}$=34 kJ mol^{-1}). This reaction is highly exergonic (ΔG=-234 kJ mol^{-1}), and the C–C bond in the CHOCOO* product can be readily broken to form CO_2 (Fig. 3; TS6, $\Delta E^{\ddagger}$=-312, $\Delta G^{\ddagger}$=-222 kJ mol^{-1}). The remaining CHO* fragment can react with another O_2 molecule to produce additional CO_2 and an OH* adsorbate that

can complete the catalytic cycle by facilitating the formation of a new CH_3COO* from a co-adsorbed CH_3COOH*. In experiments, CO pressures are inversely proportional to fed O_2 pressure, suggesting that low O_2 pressures favor non-oxidative dehydrogenation of CHO*, forming CO* that can desorb in steps that do not affect the overall acetate decomposition rate.

Thus, the kinetically relevant transition states that form decomposition products from CH_3COO* can be oxidative or non-oxidative, with the oxidative step involving abstraction of Pd-bound H* by O_2*, and the non-oxidative step involving H transfer to a vicinal CH_3COO* after a lower-energy C–H activation in CH_3COO* by a Pd atom. Although the barrier for abstraction of H* by O_2* is slightly higher than the O_2*-assisted C–H activation barrier in Fig. 3 (TS4 vs. TS2, $\Delta G^{\ddagger}$=81 vs. 78 kJ mol^{-1}), higher-accuracy electronic energy calculations with an extra Pd layer in the Pd(111) slab, used to refine the barrier values for potentially kinetically relevant steps, show that TS4 has a lower barrier than TS2 ($\Delta G^{\ddagger}$=81 vs. 93 kJ mol^{-1}) and is therefore the kinetically relevant oxidative step at 6/16. These calculations are described in the computational methodology (SI, section S1), and differences in barriers between lower- and higher-accuracy methods are tabulated in the SI (Table S5).

Decomposition of Ethylene at 6/16 Coverage

Scheme 3. Plausible oxidative (orange arrows) and non-oxidative (black arrows) steps involved in the conversion of ethylene-derived species to undesired products. Bold arrows show the most favored paths. Relevant transition states labeled with double-dagger symbols are found in Fig. 4 (TS8–TS10) or the SI (Fig. S2 and S9).

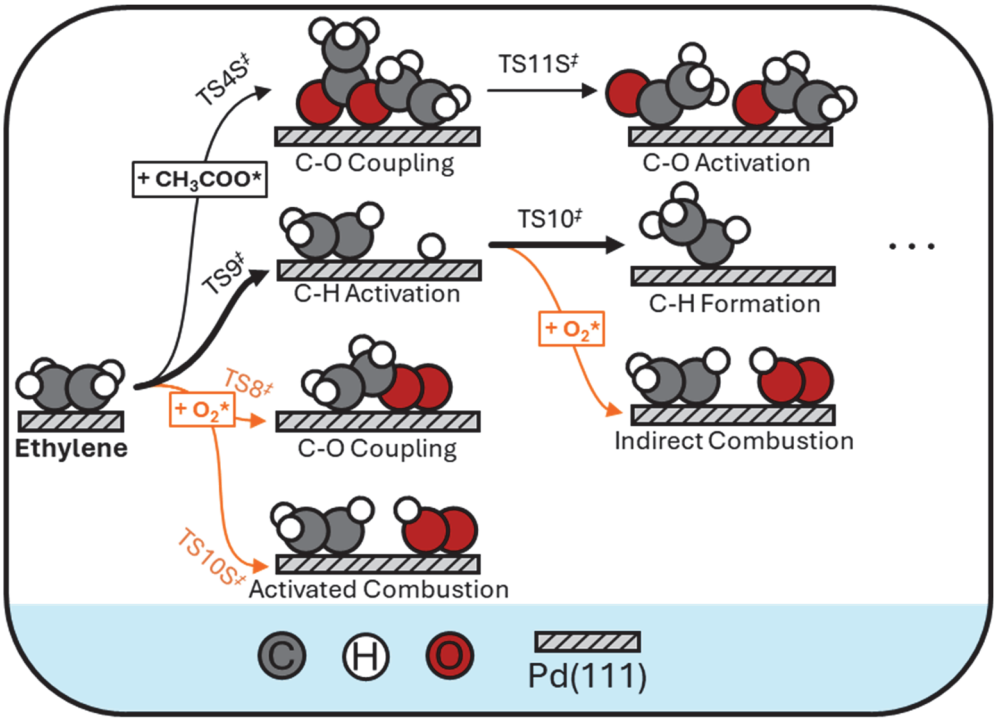

Scheme 3 shows possible initial steps in non-oxidative and oxidative decomposition routes for C_2H_4. A non-oxidative route can involve C–O cleavage in the acetoxyethyl intermediate formed by CH_3COO*–C_2H_4* coupling in the selective VA synthesis pathway. Previous surface science analysis on Pd(100) suggests that CO formation during VA synthesis can occur through this C–O activation.[32] This step also produces an acetyl group that could combine with an H* to form the trace acetaldehyde observed in experiments; however, we found that the transition state for this C–O activation at 6/16 coverage is too unstable to be a significant C_2H_4* or CH_3COO* decomposition path, as shown in the SI (Fig. S9, TS11S, $\Delta E^{\ddagger}$=43, $\Delta G^{\ddagger}$=155 kJ mol^{-1}). C_2H_4* can also decompose through a non-oxidative C–H activation, depositing an H* species on the Pd atoms at a vicinal CH_3COO* vacancy site. This C–H activation is much more facile (Fig. 4, black line; TS9, $\Delta E^{\ddagger}$=3, $\Delta G^{\ddagger}$=97 kJ mol^{-1}) and initiates the dehydrogenation of C_2H_4* to CCH_3*, known to be rapid on Pd(111).[28,39-41] After C–H activation of C_2H_4*, the product H* recombines onto the vinyl species to form $CHCH_3$* (TS10, $\Delta E^{\ddagger}$=7, $\Delta G^{\ddagger}$=88 kJ mol^{-1}); finally, another C–H activation produces H* and CCH_3* (TS11, $\Delta E^{\ddagger}$=-31, $\Delta G^{\ddagger}$=78 kJ mol^{-1}).

Alternatively, an O_2 molecule can adsorb at a vicinal acetate vacancy and react with C_2H_4* through C–O coupling to form an oxametallacycle-like $CH_2CH_2O_2$* species (Fig. 4, orange dashed line; TS8, $\Delta E^{\ddagger}$=-47, $\Delta G^{\ddagger}$=158 kJ mol^{-1}). Although interactions between the Pd surface and C_2H_4*

and O_2* decrease electronic energy, the surface-adsorbate interactions at this high coverage are not strong enough to counteract entropic increases for both additional co-adsorbates, making this oxidative transition state unfavorable. O_2*-assisted C–H activation of C_2H_4* has an even more unstable transition state, as shown in the SI (Fig. S9, TS10S, $\Delta E^{\ddagger}$=-24, $\Delta G^{\ddagger}$=178 kJ mol^{-1}).

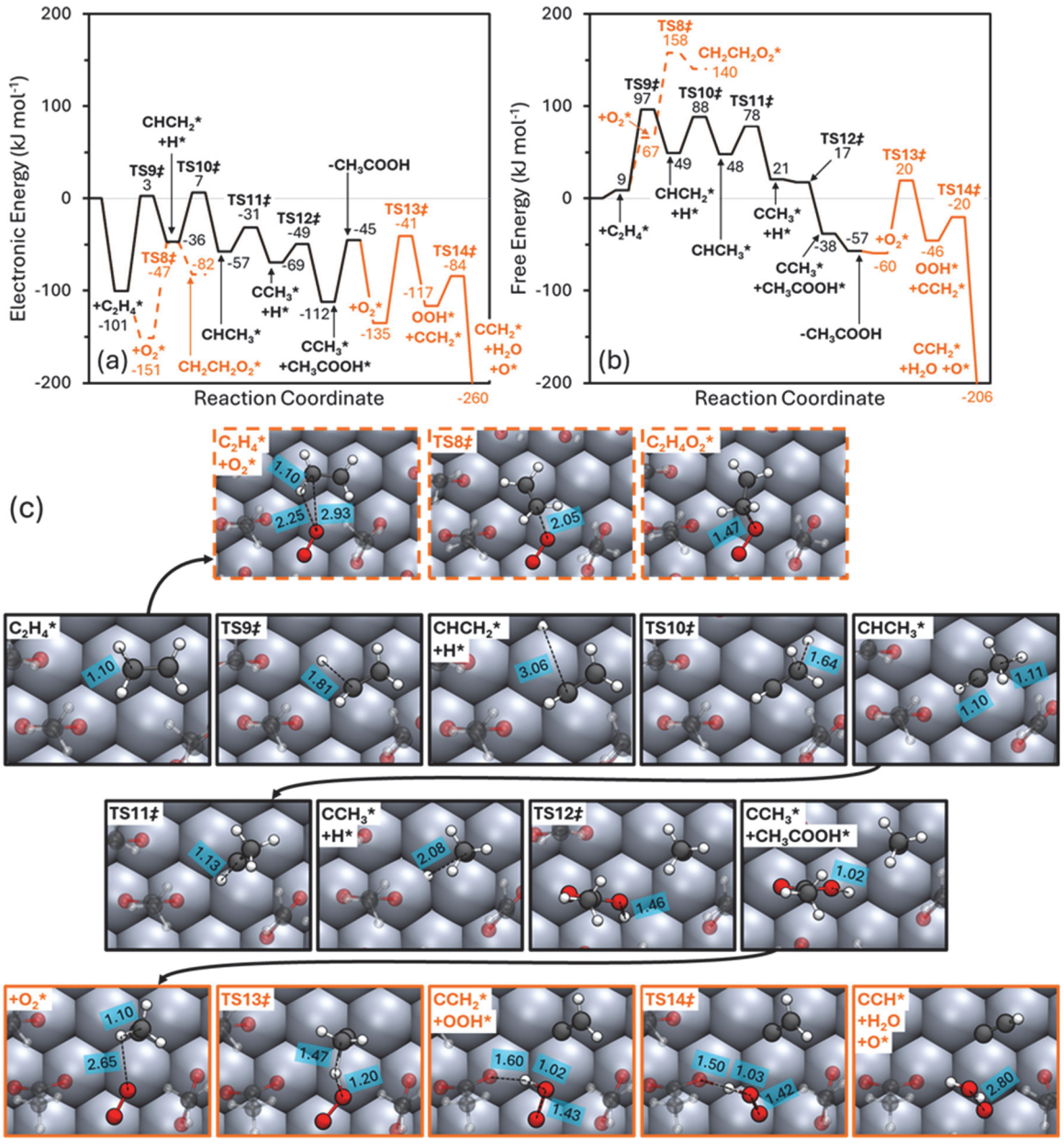

Figure 4. PBE-D3BJ-derived (a) electronic energies, (b) Gibbs free energies at 433K and 10 kPa gaseous reactants, and (c) structures for intermediates and transition states involved in non-oxidative (black) and oxidative (orange) decomposition of C_2H_4* at 6/16 surface coverage. Bond

distances shown in Å; spectator acetates shown as transparent structures. Corresponding energy, enthalpy, entropy, and free energy are tabulated in the SI (Table S2).

After dehydrogenation of C_2H_4* to CCH_3*, the product H* can undergo barrierless O–H formation with an adjacent CH_3COO* to form CH_3COOH* (Fig. 4; TS12, $\Delta E^{\ddagger}$=-49, $\Delta G^{\ddagger}$=17 kJ mol^{-1}). The desorption of this CH_3COOH* is exergonic (-19 kJ mol^{-1} free energy change) and is followed by O_2 adsorption near the CCH_3* species (Fig. 4, orange line; -3 kJ mol^{-1}). O_2* then abstracts an H atom from CCH_3* (Fig. 4; TS13, $\Delta E^{\ddagger}$=-41, $\Delta G^{\ddagger}$=20 kJ mol^{-1}), and the reactive OOH* product rapidly abstracts an additional H from CCH_2*, forming H_2O (Fig. 4; TS14, $\Delta E^{\ddagger}$=-84, $\Delta G^{\ddagger}$=-20 kJ mol^{-1}). The CCH* fragment can couple with the remaining O*, then rapidly undergo oxidation to CO_2, eventually leaving only an OH* adsorbate that can complete the catalytic cycle, as in the CH_3COO* decomposition case, by facilitating the formation of a new CH_3COO* from a co-adsorbed CH_3COOH*. As with CH_3COO* decomposition, the source of experimentally observed CO is likely from O_2-scarce conditions that inhibit oxidation of CO to CO_2 but do not substantially affect decomposition rates.

Catalytic Cycle and Effects of Acetate Coverage on Activation Barriers

Scheme 4. A catalytic cycle involving steps for acetate formation (blue), VA formation (red) and decomposition (black - non-oxidative steps, orange – oxidative steps) from surface acetate and ethylene species. Each asterisk represents a Pd atom pair. ^ represents a kinetically relevant step.

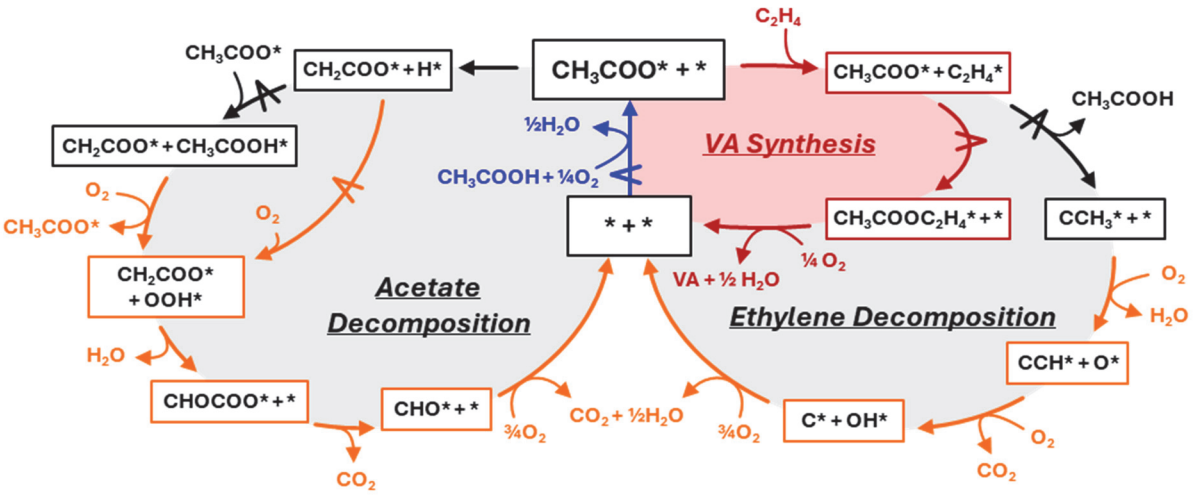

Based on these DFT calculations, we propose the catalytic cycle shown in Scheme 4. In this cycle, the reference state is a particular CH_3COO^* coverage with a vicinal vacancy ($CH_3COO^* + *$). New CH_3COO^* species can form at vacant sites to increase the coverage (blue path). Alternatively, C_2H_4 can bind at the vacancy site and couple with CH_3COO^* to form VA (red path), which desorbs to decrease CH_3COO^* coverage. At conditions where the barriers for CH_3COO^* formation steps are lower than the barriers for CH_3COO^* consumption steps, CH_3COO^* coverage will increase, setting the steady-state CH_3COO^* coverage to values where the formation and consumption steps have similar barriers such that both can occur at the same rate at a given set of reactant pressures. Previous DFT calculations showed that CH_3COO^* formation is much more rapid than its consumption via VA formation at low coverages, but the two barriers become similar near 6/16 coverage.[30] These steps were calculated here with more stable configurations of spectator acetates, leading to the same conclusion but lower barriers, as shown in the SI (Figs. S1–S3). The VA formation catalytic cycle is expanded here to include decomposition steps that limit VA selectivity (Scheme 4). This expanded cycle includes additional decomposition paths for CH_3COO^* consumption, as well as C_2H_4 adsorption and decomposition paths. In the decomposition path for CH_3COO^*, the kinetically relevant step involves transfer of Pd-bound H* either to a vicinal CH_3COO^* (non-oxidative) or a vicinal O_2^* (oxidative), while for $C_2H_4^*$ the only kinetically relevant step is initial C–H activation (non-oxidative).

To determine the effect of coverage on the decomposition barriers, the steps described for 6/16 coverage in Figs. 3 and 4 were calculated for 5/16 and 7/16 coverage, as shown in detail in Figs. S9-S12. In brief, initial C–H activation is the rate-limiting step for $C_2H_4^*$ decomposition at all coverages, with all oxidative steps being kinetically irrelevant. For CH_3COO^*, initial C–H activation is rate-limiting at 5/16 coverage, while above this coverage the transfer of Pd-bound H* to a vicinal CH_3COO^* is the kinetically relevant non-oxidative step. Compared to these non-oxidative steps, oxidative decomposition steps for CH_3COO^* have very similar barriers at 5/16 and 6/16 (e.g. Fig. 3, TS3 within 5 kJ mol^{-1} of TS4) but much higher barriers at 7/16 coverage.

The electronic energies of kinetically relevant steps for CH_3COO^* formation, VA formation, oxidative and non-oxidative CH_3COO^* decomposition, and non-oxidative $C_2H_4^*$ decomposition were calculated with higher computational accuracy and an additional Pd layer in the Pd(111) slab to obtain final, more accurate activation barriers (as described in the computational methodology in the SI, section S1). The effects of the calculation method accuracy

on electronic and free energies for the kinetically relevant decomposition paths are tabulated in the SI (Table S5). Fig. 5 presents trends in the DFT-derived reaction barriers with surface coverage, referenced to the surface with unoccupied vacancies as shown in Fig. 2 for each coverage and 10 kPa gaseous reactants at 433 K.

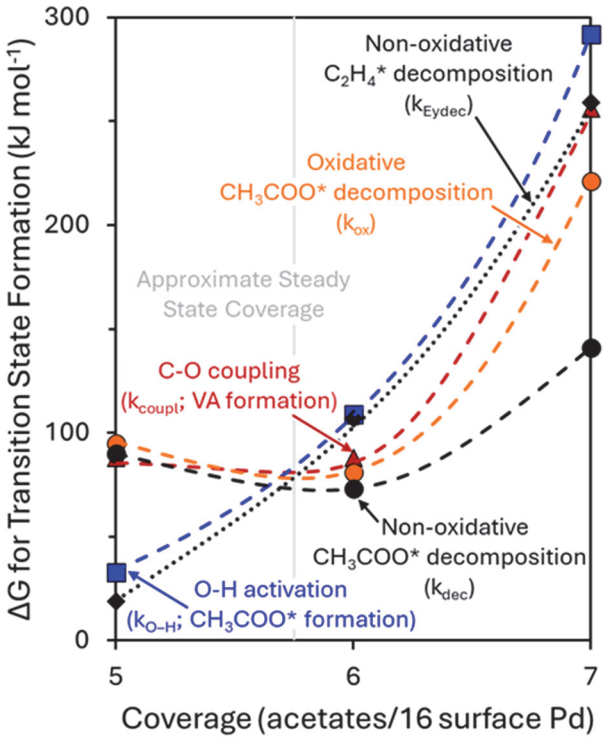

Figure 5. PBE-D3BJ-derived Gibbs free energy barriers referenced to the CH_3COO^* covered surface with vicinal vacancies at 433 K and 10 kPa gaseous reactants as a function of surface CH_3COO^* coverage for acetate formation, VA formation, oxidative and non-oxidative CH_3COO^* decomposition and non-oxidative $C_2H_4^*$ decomposition. Dashed lines show trends. Calculations for C–O coupling and O–H activation are shown in the SI (Fig. S1).

At 5/16 CH_3COO^* coverage, the non-oxidative $C_2H_4^*$ decomposition barrier referenced to a vacant site and gaseous C_2H_4 is only 19 kJ mol^{-1}, but it increases strongly with increasing coverage, which in turn reflects the strong sensitivity of C_2H_4 adsorption to adsorbate-adsorbate repulsion. The CH_3COO^* formation barrier is similarly low at 5/16 coverage (33 kJ mol^{-1}) and exhibits similar strong coverage dependence. The CH_3COO^* species formed rapidly with these low barriers accumulate on the surface because all CH_3COO^* consumption steps have much higher barriers (> 88 kJ mol^{-1}) at 5/16 coverage. In contrast, $C_2H_4^*$ decomposition forms CO_2 that can

desorb. This CH_3COO^* accumulation leads to higher steady-state coverages where additional CH_3COO^* formation and $C_2H_4^*$ decomposition steps are less facile.

In contrast to CH_3COO^* formation and $C_2H_4^*$ decomposition, the VA formation barrier is essentially independent of coverage between 5/16 and 6/16. This weak dependence likely reflects a balance between weaker C_2H_4 binding and greater C–O coupling propensity for more labile species, especially because the coupling transition state takes less surface area than $CH_3COO^*+C_2H_4^*$ precursors and consequently decreases the inter-adsorbate repulsion at 6/16. Above 6/16, this barrier increases, as the adsorption of C_2H_4 near CH_3COO^* becomes strongly inhibited by surface crowding. Similarly, oxidative CH_3COO^* decomposition is nearly independent of coverage between 5/16 and 6/16 but becomes unfavorable as coverage increases above 6/16 and O_2 co-adsorption is inhibited. The non-oxidative CH_3COO^* decomposition barrier exhibits similar trends as the oxidative barrier between 5/16 and 6/16, but is less inhibited moving from 6/16 to 7/16, because this decomposition transition state does not require additional adsorbates or a much larger area than the precursor CH_3COO^* species.

The steady state coverage, at which rates of acetate formation and consumption are equal, is about 5.75/16, marked on Fig. 5 by a pale gray vertical line. At this coverage, the VA formation barrier is similar to the CH_3COO^* and $C_2H_4^*$ decomposition barriers, which is consistent with the moderate VA selectivity observed in experiments. The barriers in Fig. 5 are for 10 kPa C_2H_4, CH_3COOH, and O_2, and a change in reactant pressure can modify the steady state coverage, but only a narrow coverage range is accessible for steady state experiments because the CH_3COO^* formation barrier changes strongly with coverage to counteract pressure changes. Over the narrow accessible coverage range, increasing coverage strongly inhibits $C_2H_4^*$ decomposition but minimally affects the barriers for VA formation or for oxidative or non-oxidative CH_3COO^* decomposition, and therefore increases selectivity. To test if these DFT-derived insights and barrier trends correspond well to the measured selectivity trends, and to more thoroughly investigate how reactant pressures affect the formation of decomposition products, we turn to experimental validation of the proposed reaction steps.

Measured VA Selectivity and Regressed Kinetic Parameters

As shown in Fig. 1, the measured VA selectivity is not affected by VA product accumulation with increasing residence time, which suggests that secondary reactions of the primary product are

negligible for the measurement conditions used. Therefore, the selectivity depends solely on the ratio of the rate of primary VA formation to rates of parallel primary reactions forming byproducts via parallel CH_3COO^* and $C_2H_4^*$ decomposition (r_{VA}/r_{BP}). A kinetic expression for this rate ratio can be derived from a series of elementary steps shown in Scheme 5 that are consistent with the DFT calculations (Figs. 3, 4) and the resulting catalytic cycle (Scheme 4).

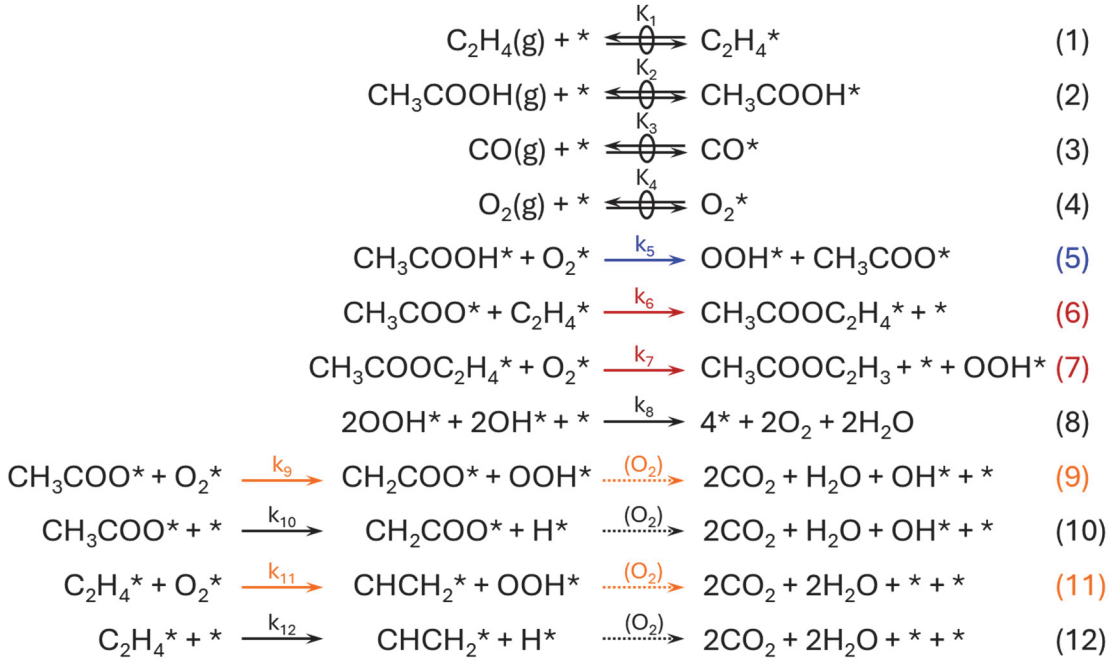

Scheme 5. Proposed steps consistent with DFT-derived paths and kinetically relevant transition states for VA synthesis, acetate decomposition and ethylene decomposition cycles in Scheme 4. Dotted arrows in steps 9-12 represent multiple elementary steps initiated by the listed reactants and are not stoichiometrically balanced. Blue, red, and orange arrows represent acetate formation, acetate consumption to form VA, and O_2-mediated decomposition, respectively.

Scheme 5 includes elementary steps for molecular adsorption of reactants and CO molecules (steps 1-4), CH_3COO^* formation via H-abstraction from CH_3COOH^* by O_2 (step 5), CH_3COO^*–$C_2H_4^*$ coupling to form an acetoxyethyl intermediate (step 6), an H-abstraction from acetoxyethyl by O_2 to form VA (step 7), and consumption of OOH^* species (step 8), as previously identified in mechanistic analysis for VA formation.[30] Additionally, the scheme includes elementary steps for initial oxidative and non-oxidative activations of CH_3COO^* (steps 9-10) and

C_2H_4* (steps 11-12), followed by a rapid non-elementary transformations leading to CO_2. These steps and the pseudo-steady-state approximation were used to derive expressions for CH_3COO* coverage and rates of formation of VA and decomposition of CH_3COO* and C_2H_4* as shown in the SI (Section S16). The ratio of the coverages of acetates and acetate vacancies ([CH_3COO*]/[*]) is given by a ratio of the rate of CH_3COO* formation (step 5, Scheme 5) to the sum of rates of CH_3COO* consumption by coupling with C_2H_4* and oxidative and non-oxidative decompositions (steps 6, 9, 10) in the following expression:

$$\frac{[CH_3COO*]}{[*]} = \frac{k_{O-H}P_{CH_3COOH}P_{O_2}}{k_{coupl}P_{C_2H_4}+k_{ox}P_{O_2}+k_{dec}} = \frac{\frac{k_{O-H}P_{CH_3COOH}P_{O_2}}{k_{coupl}P_{C_2H_4}}}{1+\frac{k_{ox}P_{O_2}}{k_{coupl}P_{C_2H_4}}+\frac{k_{dec}}{k_{coupl}P_{C_2H_4}}} \quad (1)$$

Here, the rate parameter k_{O-H} is related to the free energy of the transition state for acetate formation (TS2S, Fig. S1), referenced to two vacant sites and gaseous CH_3COOH and O_2, through the form of the Eyring equation:

$$k_{O-H} = k_5K_2K_4 \sim \exp[-(G^{\ddagger}_{TS2S} - G_{*+*} - G_{CH_3COOH(g)} - G_{O_2(g)})/RT] \quad (2)$$

k_{coupl} reflects the free energy of the transition state for acetoxyethyl formation by C–O coupling (leading to VA, TS4S, Fig. S2) referenced to a vacant site, a surface acetate, and gaseous C_2H_4:

$$k_{coupl} = k_6K_1 \sim \exp[-(G^{\ddagger}_{TS4S} - G_{CH_3COO*+*} - G_{C_2H_4(g)})/RT] \quad (3)$$

k_{ox} reflects the free energy of the transition state for oxidative acetate decomposition (TS4, Fig. 3; high-accuracy calculations show TS4 preferred to TS2; see Table S5) referenced to a vacant site, a surface acetate, and gaseous O_2:

$$k_{ox} = k_9K_4 \sim \exp\left[-\left(G^{\ddagger}_{TS4} - G_{CH_3COO*+*} - G_{O_2(g)}\right)/RT\right] \quad (4)$$

and k_{dec} reflects the free energy of the transition state for non-oxidative CH_3COO* decomposition (TS3, Fig. 3) referenced to a vacant site and a surface acetate:

$$k_{dec} = k_{10} \sim \exp[-(G^{\ddagger}_{TS3} - G_{CH_3COO*+*})/RT] \quad (5)$$

Equation 1 suggests that the [CH_3COO*]/[*] ratio increases linearly with CH_3COOH pressure; exhibits a Langmuir-type increase with O_2 pressure, with decreasing sensitivity at higher pressure; and decreases with C_2H_4 pressure. The kinetic parameters k_{O-H}, k_{coupl}, k_{ox} and k_{dec} typically treated as constants in such expressions also depend strongly on coverage, as shown by corresponding free energy barriers in Fig. 5. This recursive dependence gives a more complex self-consistent dependence of coverage on pressure, making the accessible Langmuirian coverage range of 0 to 1 a much narrower range of actual coverages where acetates are labile for

consumption because acetate formation and consumption barriers are similar.[30] The VA formation rate, given by the CH_3COO*–C_2H_4 coupling rate, can be expressed as (details in SI, Section S16):

$$\frac{r_{VA}}{[L]} = \frac{\frac{[CH_3COO*]}{[*]} k_{coupl} P_{C_2H_4}}{\left(1 + K_3 P_{CO} + K_4 P_{O_2} + \frac{[CH_3COO*]}{[*]}\right)^2} \quad (6)$$

where $[L]$ is the total number of sites, and the denominator terms on the right-hand side reflect ratios of coverages of significant surface species to that of vacancies, with K_3 and K_4 being equilibrium parameters for the adsorption of CO (formed as a minor byproduct but adsorbs strongly) and O_2, respectively.

CH_3COO* and C_2H_4* decompositions occurring at the same coverage have the same denominator terms in their rate expressions as Equation 6, giving the following form for the r_{VA}/r_{BP} rate ratio relevant for selectivity (detailed derivation in SI, Section S16):

$$\frac{r_{VA}}{r_{BP}} = \frac{\frac{[CH_3COO*]}{[*]} k_{coupl} P_{C_2H_4}}{\frac{[CH_3COO*]}{[*]} k_{ox} P_{O_2} + \frac{[CH_3COO*]}{[*]} k_{dec} + k_{Eyox} P_{C_2H_4} P_{O_2} + k_{Eydec} P_{C_2H_4}} \quad (7)$$

where the denominator terms in Equation 7, in the order of their appearance, reflect the rates of oxidative CH_3COO* decomposition, non-oxidative CH_3COO* decomposition, oxidative C_2H_4* decomposition, and non-oxidative C_2H_4* decomposition. This expression can be rearranged to the following form in which the ratio of the decomposition rate parameters to k_{coupl}, along with reactant pressures, become the determinants of the selectivity:

$$\frac{r_{VA}}{r_{BP}} = \frac{1}{\left(\frac{k_{ox} P_{O_2}}{k_{coupl} P_{C_2H_4}} + \frac{k_{dec}}{k_{coupl} P_{C_2H_4}}\right) + \frac{[*]}{[CH_3COO*]}\left(\frac{k_{Eyox} P_{O_2}}{k_{coupl}} + \frac{k_{Eydec}}{k_{coupl}}\right)} \quad (8)$$

Here, the rate constant k_{Eyox} represents the free energy of the transition state for oxidative C_2H_4* decomposition (TS8, Fig. 4) referenced to a vacant site, a surface acetate, and gaseous C_2H_4 and O_2:

$$k_{Eyox} = k_{11} K_4 / K_1 \sim \exp[-(G^{\ddagger}_{TS8} - G_{CH_3COO*+*} - G_{C_2H_4(g)} - G_{O_2(g)})/RT] \quad (9)$$

and the rate constant k_{Eydec} is the free energy of the transition state for non-oxidative C_2H_4* decomposition (TS9, Fig. 4) referenced to a vacant site, a surface acetate, and gaseous C_2H_4:

$$k_{Eydec} = k_{12} / K_1 \sim \exp[-(G^{\ddagger}_{TS9} - G_{CH_3COO*+*} - G_{C_2H_4(g)})/RT] \quad (10)$$

Equations 1, 6, and 8 together describe rate and selectivity dependence on reactant pressures, expanding an earlier framework describing only VA rates. Experimental rate and selectivity data were regressed simultaneously to the forms of these equations. Fig. 6 shows

measured and regressed selectivity, represented as the rate ratio r_{VA}/r_{BP}, as a function of C_2H_4, CH_3COOH and O_2 pressures, and the regression parameters are shown in Table 1. Measured and regressed rates are included in the SI (Fig. S15). k_{Eyox} was removed from the regression, as its value was nearly zero and its standard error greater than its value. Its exclusion reduces the uncertainty for other parameters in Equation 8 without substantially changing their values (Table S6 in the SI). This supports the conclusion from DFT that C_2H_4 decomposition paths with kinetically relevant oxidative steps do not contribute significantly to the unselective products in VA synthesis on Pd. Rate ratios are near or below 1 at most reaction conditions, suggesting that decomposition rates are greater than or similar to the VA formation rate on monometallic Pd at these conditions.

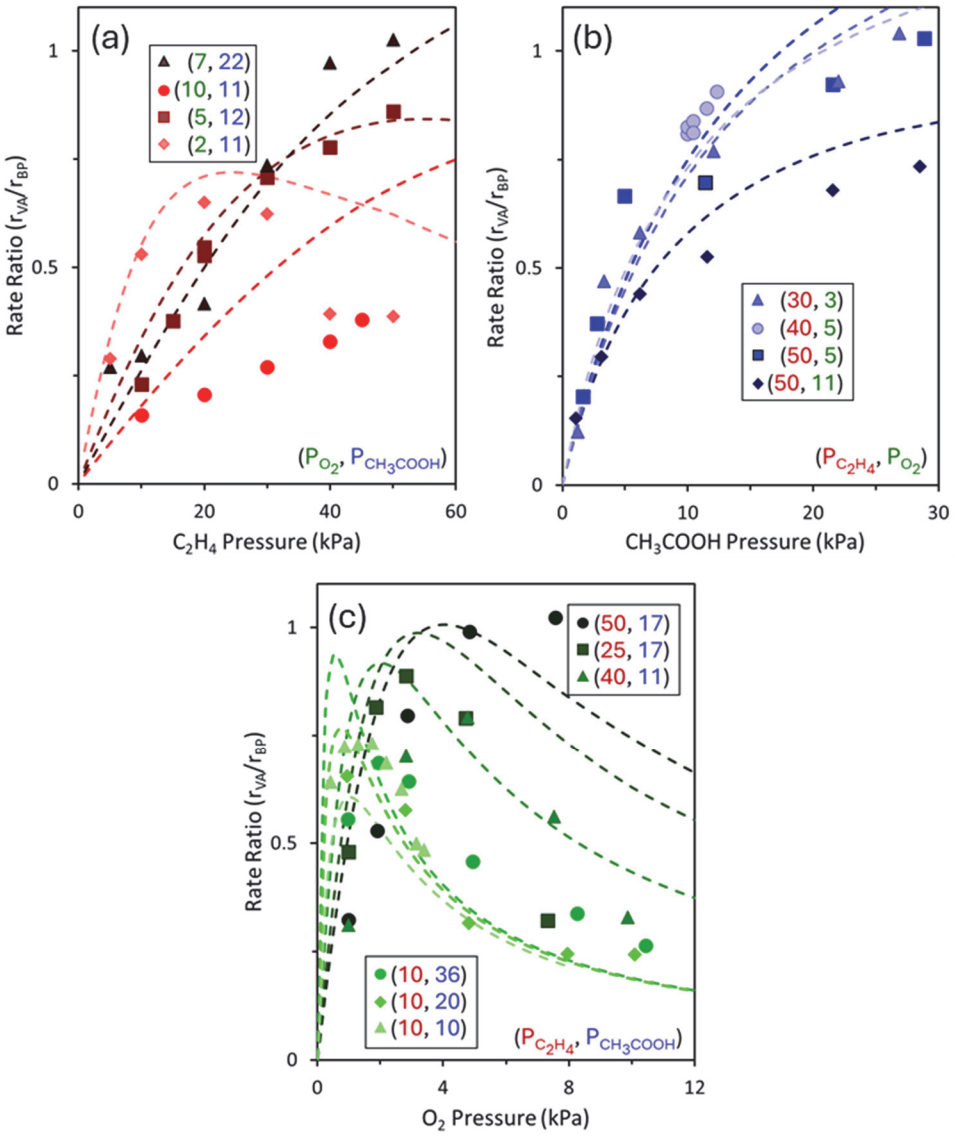

Figure 6. Measured selectivity represented as the ratio of the rates of VA and byproduct formation (r_{VA}/r_{BP}) as a function of (a) C_2H_4 pressure, (b) CH_3COOH pressure, and (c) O_2 pressure at 433 K on 1 wt. % Pd/SiO_2. Legends show fixed pressures of other reactants. Dashed lines show best fits to the form of Equation 8. Parity plots and measured VA formation rates of measured and fit-predicted rates and selectivity are shown in the SI (Figs. S14–S15).

Table 1. Rate and selectivity parameters derived from regression of experimental rates and selectivity to the forms of Equations 6 and 8.

Parameter	Value	Std. Err.	Units
K_3	87.9	16.2	kPa^{-1}

K_4	0.45	0.09	kPa^{-1}
$k_{O–H}$	0.95	0.28	$Pd^{-1}\ ks^{-1}$
$k_{O–H}$ / k_{coupl}	0.51	0.11	kPa^{-1}
k_{ox} / k_{coupl}	4.76	0.40	–
k_{dec} / k_{coupl}	4.78	1.23	kPa
k_{Eyox} / k_{coupl}	0	–	kPa^{-1}
k_{Eydec} / k_{coupl}	0.26	0.06	–

Fig. 6a shows the effects of C_2H_4 pressure on the rate ratio for four datasets with different fixed CH_3COOH and O_2 pressures. The selectivity increases with C_2H_4 pressure at low pressures but decreases at high pressures. Three of the datasets use similar CH_3COOH pressures (11-12 kPa) to illustrate how C_2H_4 pressure affects selectivity at different O_2 pressures. The data show that increasing O_2 pressure from 2 kPa to 5 kPa increases the C_2H_4 pressure at which selectivity begins to decrease. Increasing O_2 pressure further to 10 kPa increases this inversion pressure further but decreases the overall selectivity. The fourth dataset uses a moderate O_2 pressure of 7 kPa and a higher CH_3COOH pressure of 22 kPa and shows that increasing CH_3COOH pressure tends to increase the overall selectivity.

Fig. 6b shows the effects of CH_3COOH pressure on rate ratios for four datasets with different fixed C_2H_4 and O_2 pressures. Selectivity increases monotonically with CH_3COOH pressure for all conditions. Three of the four datasets use similar O_2 pressures (3-5 kPa) to illustrate how CH_3COOH pressure affects selectivity at different C_2H_4 pressures. The data show that increasing C_2H_4 pressure from 30 to 50 kPa has little effect on the trends; however, increasing O_2 pressure to 11 kPa while maintaining 50 kPa C_2H_4 causes the selectivity to decrease substantially.

Fig. 6c shows six datasets with different fixed C_2H_4 and CH_3COOH pressures. Similarly to trends for C_2H_4 pressures, the selectivity increases with O_2 pressure at low pressures but decreases at high pressures. This inversion occurs at a much lower O_2 pressure than it does for C_2H_4 pressures. Two datasets in Fig. 6c use identical CH_3COOH pressure (17 kPa) to illustrate how O_2 pressure affects selectivity at different C_2H_4 pressures. The two datasets have similar selectivity at low O_2 pressures; however, selectivity inverts at a higher O_2 pressure and the maximum selectivity is higher when C_2H_4 pressure is higher (50 vs. 25 kPa). Two more datasets use similar, lower CH_3COOH pressures (10-11 kPa). These datasets show that a change from 10 kPa C_2H_4 to 40 kPa C_2H_4 causes selectivity to increase substantially except at very low O_2 pressures (< 2 kPa) and causes inversion to occur at a higher O_2 pressure. Overall selectivity for

these datasets is lower than for the first two datasets due to decreased CH_3COOH pressure. Three datasets use identical C_2H_4 pressure (10 kPa) and show that increasing CH_3COOH pressure from 10 to 30 kPa increases selectivity without changing the O_2 pressure at which selectivity inverts.

The tendency of selectivity to invert from positive trends to negative trends at high C_2H_4 or high O_2 pressures and the dependence of this inversion pressure on the pressure of the other reactant are explained by Equations 1 and 8, which show that coverage and selectivity depend on the O_2:C_2H_4 pressure ratio. Fig. 7 shows C_2H_4 and O_2 pressure effects for measured rates (Figs. S15a, S15c) and rate ratio (Figs. 6a, 6c), condensed and shown as a function of O_2:C_2H_4 pressure ratio. For all conditions, Fig. 7b shows that selectivity to VA rapidly increases with O_2:C_2H_4 ratio at low ratios, then inverts at a ratio of approximately 0.1 and decreases with increasing ratio. This inversion behavior can be explained by the forms of Equations 1 and 8: at low O_2:C_2H_4 ratios, CH_3COO* coverage decreases (Equation 1), which leaves C_2H_4 decomposition as the dominant reaction, as its contribution to byproducts is inversely proportional to the coverage term [CH_3COO*]/[*] (Equation 8). Increasing the O_2:C_2H_4 ratio to small values around 0.1 increases coverage, driving the VA formation necessary for higher selectivity. However, high ratios mean either that O_2 pressure is high, in which case the oxidative CH_3COO* decomposition term in Equation 8 increases, or C_2H_4 pressure is low, in which case the VA formation rate and C_2H_4* decomposition rate decrease.

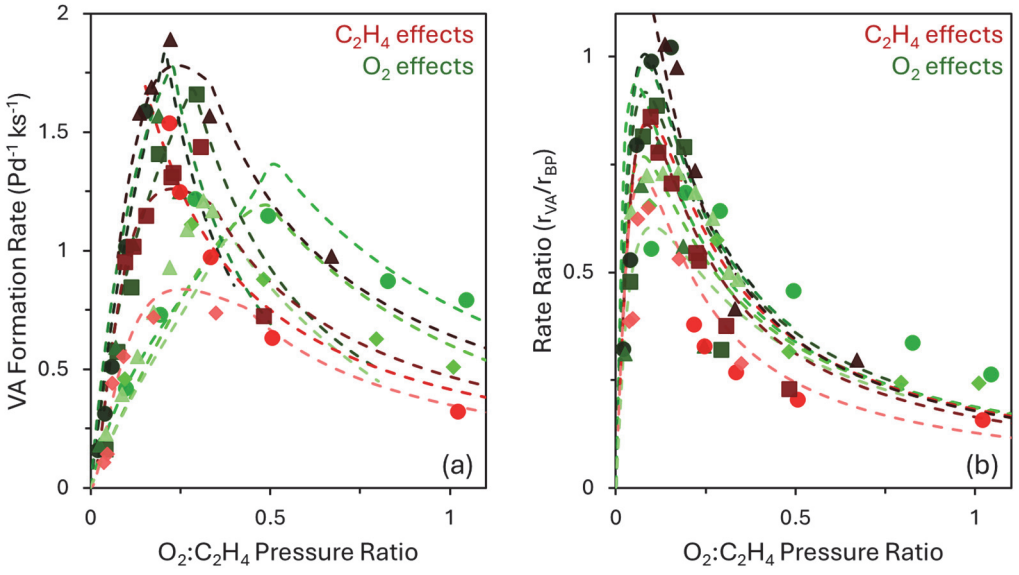

Figure 7. Measured (a) VA synthesis rate and (b) selectivity represented as a ratio of rates of VA and byproducts formation (r_{VA}/r_{BP}) as a function of O_2:C_2H_4 pressure ratio at 433 K on 1 wt. %

Pd/SiO_2. While maintaining other conditions constant, the green points and lines show the effects of changing O_2 pressure and red points and lines show the effects of changing C_2H_4 pressure. Dashed lines show best fits to the form of Equation 8. Parity plots of measured and fit-predicted rates and selectivity are shown in the SI (Fig. S14).

The sharp nature of the inversion of selectivity near an O_2:C_2H_4 pressure ratio of 0.1 suggests that decomposition products are formed through kinetically relevant oxidative steps except when O_2 pressure is over an order of magnitude lower than C_2H_4 pressure. Since C_2H_4 decomposition through kinetically relevant oxidative steps is insignificant (Table 1, $k_{Eyox} = 0$), CH_3COO* must contribute to most oxidative decompositions. Fig. 8 shows the relative magnitude of the three decomposition paths (non-zero denominator terms in Equation 8) at representative reaction conditions with 5 kPa CH_3COOH (Fig. 8a) and 25 kPa CH_3COOH (Fig. 8b).

Fig. 8a shows that, at low CH_3COOH pressures and high C_2H_4 pressures, most of the decomposition products arise from C_2H_4 at low O_2 pressure (darker lines), but rising O_2 pressure (lighter lines) causes the C_2H_4 contribution to decrease as the rate of oxidative CH_3COO* decomposition rises. Contribution from non-oxidative CH_3COO* decomposition also decreases as O_2 pressure rises because the P_{O_2} factor in the rate of oxidative CH_3COO* decomposition makes it more significant at higher O_2 pressure (Equation 8). As CH_3COOH pressures increase to 25 kPa (Fig. 8b), these trends remain similar, but the relative contributions of the CH_3COO* decomposition pathways increase due to increasing coverage. At this higher CH_3COOH pressure, C_2H_4* decomposition dominates only when O_2 pressure is very low (≤3 kPa) and C_2H_4 pressure is very high (>40 kPa). Under most reaction conditions, oxidative CH_3COO* decomposition is the primary route for the production of unselective products in VA synthesis.

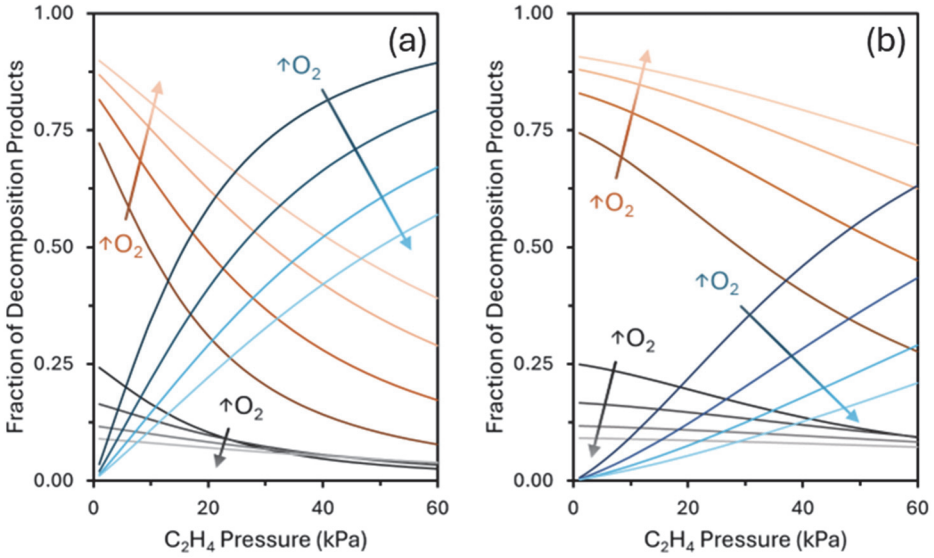

Figure 8. Contributions to decomposition products from oxidative (orange), non-oxidative (gray) CH_3COO^*, and non-oxidative C_2H_4 (blue) activations as predicted from kinetic parameters in Table 1, as a function of C_2H_4 pressure at (a) 5 kPa CH_3COOH and (b) 25 kPa CH_3COOH. Lighter colors correspond to higher O_2 pressures, with lines showing 3, 5, 7.5, and 10 kPa O_2. Calculation details are shown in the SI (Section S20).

The trends in Figure 8 arise from the numerical values of the regressed kinetic parameters shown in Table 1, which can be compared with the trends in DFT-derived reaction barriers to determine how closely experiments and computation agree. The rate parameter ratios k_x/k_{coupl} (k_x=k_{O-H}, k_{ox}, k_{dec}, k_{Eydec}) in Table 1 reflect the differences in the free energies of the kinetically relevant transition states for the paths representing the k_x values and the transition state for the C–O coupling (VA formation) path:

$$\frac{k_x}{k_{coupl}} = \exp\left(\frac{\Delta G^{\ddagger}_{coupl} - \Delta G^{\ddagger}_{x}}{RT}\right)\left(P_{ref}\right)^{\delta} = \exp\left(\frac{\Delta\Delta G^{\ddagger}}{RT}\right)\left(P_{ref}\right)^{\delta} \quad (11)$$

where $\Delta G^{\ddagger}_{x}$ and $\Delta G^{\ddagger}_{coupl}$ reflect barriers shown in Equations 2-5 and 9-10, P_{ref} represents the reference pressure of gaseous species (1 kPa for measured values and 10 kPa for DFT-derived values), and δ is the difference in the number of gaseous species between expressions for k_{coupl} and k_x. A derivation of this equation can be found in the SI (Section S21). The $\Delta\Delta G^{\ddagger}$ values from parameters regressed to measured data (Table 1) were calculated using Equation 9, as shown in Table 2. The corresponding DFT-derived values were obtained from linear interpolation between

barriers in Figure 5 at 5/16 and 6/16 coverage to estimate values at 5.75/16 and corrected by adding $\delta RTln10$ to account for the difference in reference pressures. Table 2 shows the $\Delta\Delta G^{\ddagger}$ values from regressed parameters for measured data and from DFT.

Table 2. Free energy barrier differences ($\Delta\Delta G^{\ddagger}$) reflecting rate parameter ratios for VA formation rates and selectivity in Table 1 and corresponding DFT-derived values.

Parameter	Value	$\Delta\Delta G^{\ddagger}$ (kJ mol^{-1})		
		Measured[a]	DFT-derived	Difference
k_{O-H} / k_{coupl}	0.51 kPa^{-1}	-2.4	-9.7	-7.3
k_{ox} / k_{coupl}	4.76	5.6	3.4	-2.2
k_{dec} / k_{coupl}	4.78 kPa	5.6	18.9	13.3
k_{Eydec} / k_{coupl}	0.26	-4.8	3.7	8.5

[a] Calculated from Equation 11 and parameters in Table 1.

Table 2 shows that the $\Delta\Delta G^{\ddagger}$ values from DFT calculations differ from $\Delta\Delta G^{\ddagger}$ values from measured rate parameter ratios by -7.3 to +13.3 kJ mol^{-1}. These differences are relatively small and within typical DFT errors, which may arise from a variety of factors including selective over-binding of certain species in DFT functionals, low-frequency treatments for free energy calculation and factors involving configurational entropy and stabilities of spectator species at high coverages. Overall, the relatively small errors suggest that the extensive DFT calculations we present and the identified selectivity-limiting steps are in good agreement with mechanistic details and energetics of experimental selectivities over a wide range of reaction conditions. The results and the framework developed here can help advance a theory-led development of new VA synthesis catalysts. Specifically, we have identified key elementary steps that need to be considered to determine activity and selectivity on different surfaces and we have shown that multiple coverages need to be considered to identify conditions of steady state catalyst operation. These requirements imply that calculations at one low-coverage setting may not reflect true reactivity trends across different catalytic surfaces because the coverage-dependent barrier trends identified here will be amplified on catalysts with smaller lattice constants, as active sites will be closer, increasing inter-adsorbate repulsion. The library of structures for rate-determining transition states developed in this work can enable facile probing of alternative compositions across multiple coverages to

identify potential new catalysts that overcome the issues of instability and cost present in the Pd-based industrial catalysts while retaining high activity and selectivity.

Conclusion

We used DFT calculations at high coverages near steady state reaction conditions and analyzed measured rate and selectivity data to understand which elementary steps limit selectivity for VA synthesis reaction and how their energetics are influenced by coverage on Pd catalysts. The DFT calculations show that CH_3COO* decomposition proceeds through facile non-oxidative C–H activation of CH_3COO* to CH_2COO*, with subsequent transfer of Pd-bound H* to O_2*, either directly or after transfer to a vicinal CH_3COO*, followed by facile oxidation to CO_2. C_2H_4* decomposition proceeds by dehydrogenation to form CCH_3*, which can then be readily oxidized. Lateral inter-adsorbate repulsion caused by surface crowding at high coverages inhibits C_2H_4* decomposition strongly by inhibiting C_2H_4 adsorption and destabilizing the C_2H_4* decomposition transition state, which requires greater catalyst surface area than its initial state. Oxidative CH_3COO* decomposition is less inhibited by increasing coverage, as its rate-determining transition state takes up a similar amount of catalyst area as the initial state and because surface crowding inhibits adsorption of O_2 less than C_2H_4. Non-oxidative CH_3COO* decomposition is least inhibited by increasing coverage because its transition state takes up a similar amount of catalyst area as the initial state and no co-adsorption is required.

Such pathways and energetics derived from DFT inform proposed elementary steps and resulting equations that can describe experimental rate and selectivity data on a Pd/SiO_2 catalyst over a wide range of reaction conditions. Rate parameters derived by regressing the data to the form of kinetic equations show that both oxidative and non-oxidative rate-limiting steps contribute to decomposition products from CH_3COO*, while C_2H_4* decomposition is purely non-oxidative, in agreement with DFT-calculated barriers. At low surface coverage, corresponding to low O_2:C_2H_4 pressure ratios, C_2H_4* decomposition dominates; at higher coverage, CH_3COO* decomposition dominates, with oxidative decomposition becoming more prevalent as O_2 pressure increases. At all O_2:C_2H_4 pressure ratios, increasing CH_3COOH pressure increases the prevalence of CH_3COO* decomposition paths. Selective VA synthesis catalysis requires operation within the Goldilocks zone where the VA formation rate is maximal relative to these decomposition rates, at O_2:C_2H_4 pressure ratios of about 0.1. This comparison of theory and experiment leads to a general

framework for describing VA synthesis rate and selectivity on metallic surfaces. The general approach and the specific structures of intermediates and transition states identified in this work can be utilized to probe other catalyst compositions under realistic conditions and potentially help in prediction of more sustainable VA synthesis catalysts.

Supporting Information

The authors have cited additional references within the Supporting Information.[42-54] The SI contains: computational methodology; catalyst preparation and selectivity measurement methodology; CH_3COO^* formation and CH_3COO^*–$C_2H_4^*$ coupling barriers as a function of coverage; comparison of electronic energy barriers for C–H, C–O, and C–C activation of CH_3COO^*; tabulated energies, enthalpies, and entropies for primary decomposition pathways; energies and structures of rate-determining spans for CH_3COO^* and $C_2H_4^*$ decomposition at 7/16 coverage; energies and structures of selected unfavorable side decomposition pathways; comparison of electronic energy barriers for non-oxidative and oxidative C–H activation of CH_3COO^* at 6/16 and 1/16 coverages; nudged elastic band calculation for reaction of OOH* and CH_2COO^* at 6/16 coverage; effect of computational methods on electronic and free energies; derivation of expressions for CH_3COO^* coverage, VA synthesis rate, and rate ratio; effects of including the k_{Eyox} term in experimental regressions; parity plots for experimental regressions for rates and selectivities; experimental data and regressions for VA formation rates; equations for the relative contribution of each decomposition pathway to CO_2 production; and derivation of the equation relating rate parameter ratios to barrier free energy differences.

Acknowledgements

We are grateful to Zhaoru Zha for measuring experimental rate and selectivity data. This work was funded by an NSF CAREER award (grant# 2045675). Computational resources were provided by the Advanced Cyberinfrastructure Coordination Ecosystem: Services and Support (ACCESS) program,[55] which is supported by the National Science Foundation.

Keywords

Oxidative coupling, coverage effects, reaction mechanism, kinetics, DFT

References

[1] M. Chen, D. Kumar, C.-W. Yi, D. W. Goodman, *Science* **2005**, *310*, 291-293.

[2] S. Simson, A. Jentys, J. A. Lercher, *J. Phys. Chem. C* **2013**, *117*, 8161-8169.

[3] D. Stacchiola, F. Calaza, L. Burkholder, A. W. Schwabacher, M. Neurock, W. T. Tysoe, *Angew. Chem. Int. Ed.* **2005**, *44*, 4572-4574.

[4] P. S. Voskanyan, *Catal. Ind.* **2010**, *2*, 167-172.

[5] F. Calaza, D. Stacchiola, M. Neurock, W. T. Tysoe, *Catal. Lett.* **2010**, *138*, 135-142.

[6] R. Abel, G. Prauser, H. Tiltscher, *Chem. Eng. Technol.* **1994**, *17*, 112-118.

[7] N. Macleod, J. M. Keel, R. M. Lambert, *Appl. Catal. A: Gen.* **2004**, *261*, 37-46.

[8] D. Stacchiola, F. Calaza, L. Burkholder, W. T. Tysoe, *J. Am. Chem. Soc.* **2004**, *126*, 15384-15385.

[9] D. Kumar, M. S. Chen, D. W. Goodman, *Catal. Today* **2007**, *123*, 77-85.

[10] G. Giannakakis, Y. Soni, G. L. Novotny, Z. Zha, N. J. Libretto, Y. Dang, S. L. Suib, J. T. Miller, E. C. H. Sykes, P. Deshlahra, *J. Am. Chem. Soc.* **2024**, *146*, 20989-20995.

[11] M.-M. Pohl, J. Radnik, M. Schneider, U. Bentrup, D. Linke, A. Brückner, E. Ferguson, *J. Catal.* **2009**, *262*, 314-323.

[12] K. Motahari, G. Rempel, S. Lashkarara, K. Ghaseminezhad, A. Borumandnejad, B. Hatami, *Can. J. Chem. Eng.* **2016**, *94*, 506-511.

[13] Y. F. Han, D. Kumar, C. Sivadinarayana, A. Clearfield, D. W. Goodman, *Catal. Lett.* **2004**, *94*, 131-134.

[14] E. K. Hanrieder, A. Jentys, J. A. Lercher, *ACS Catal.* **2015**, *5*, 5776-5786.

[15] E. K. Hanrieder, A. Jentys, J. A. Lercher, *J. Catal.* **2016**, *333*, 71-77.

[16] J. J. Plata, M. García-Mota, A. A. C. Braga, N. López, F. Maseras, *J. Phys. Chem. A* **2009**, *113*, 11758-11762.

[17] M. Bowker, C. Morgan, *Catal. Lett.* **2004**, *98*, 67-67.

[18] M. Bonarowska, A. Malinowski, W. Juszczyk, Z. Karpiński, *Appl. Catal. B: Environ.* **2001**, *30*, 187-193.

[19] D. Yuan, X. Gong, R. Wu, *Phys. Rev. B* **2007**, *75*, 233401.

[20] M. S. Chen, K. Luo, T. Wei, Z. Yan, D. Kumar, C. W. Yi, D. W. Goodman, *Catal. Today* **2006**, *117*, 37-45.

[21] D. Yuan, X. Gong, R. Wu, *J. Phys. Chem. C* **2008**, *112*, 1539-1543.

[22] M. García-Mota, N. López, *J. Am. Chem. Soc.* **2008**, *130*, 14406-14407.

[23] H. W. K. Tom, C. M. Mate, X. D. Zhu, J. E. Crowell, Y. R. Shen, G. A. Somorjai, *Surf. Sci.* **1986**, *172*, 466-476.

[24] M. Gravelle-Rumeau-Maillot, V. Pitchon, G. A. Martin, H. Praliaud, *Appl. Catal. A: Gen.* **1993**, *98*, 45-59.

[25] M. Neurock, W. T. Tysoe, *Top. Catal.* **2018**, *61*, 722-735.

[26] F. Calaza, D. Stacchiola, M. Neurock, W. T. Tysoe, *Surf. Sci.* **2005**, *598*, 263-275.

[27] F. Calaza, D. Stacchiola, M. Neurock, W. T. Tysoe, *J. Am. Chem. Soc.* **2010**, *132*, 2202-2207.

[28] M. Neurock, W. T. Tysoe, *Top. Catal.* **2013**, *56*, 1314-1332.

[29] B. Samanos, P. Boutry, R. Montarnal, *J. Catal.* **1971**, *23*, 19-30.

[30] Z. Zha, P. Deshlahra, *ACS Catal.* **2021**, *11*, 1841-1857.

[31] Y. F. Han, D. Kumar, C. Sivadinarayana, D. W. Goodman, *J. Catal.* **2004**, *224*, 60-68.

[32] T. Thuening, W. T. Tysoe, *Catal. Lett.* **2017**, *147*, 1941-1954.

[33] J. M. Davidson, P. C. Mitchell, N. S. Raghavan, *Front. Chem. React. Eng.* **1984**, *1*, 300-313.

[34] E. A. Crathorne, D. Macgowan, S. R. Morris, A. P. Rawlinson, *J. Catal.* **1994**, *149*, 254-267.

[35] K. C. Chukwu, L. Árnadóttir, *J. Phys. Chem. C* **2020**, *124*, 13082-13093.

[36] K. C. Chukwu, L. Árnadóttir, *ACS Catal.* **2022**, *12*, 789-798.

[37] C. M. Rosado-Reyes, J. S. Francisco, *J. Phys. Chem. A* **2006**, *110*, 4419-4433.

[38] X.-C. Guo, R. J. Madix, *J. Am. Chem. Soc.* **1995**, *117*, 5523-5530.

[39] D. Stacchiola, W. T. Tysoe, *Surf. Sci.* **2002**, *513*, L431-L435.

[40] L. V. Moskaleva, Z.-X. Chen, H. A. Aleksandrov, A. B. Mohammed, Q. Sun, N. Rösch, *J. Phys. Chem. C* **2009**, *113*, 2512-2520.

[41] Z.-X. Chen, H. A. Aleksandrov, D. Basaran, N. Rösch, *J. Phys. Chem. C* **2010**, *114*, 17683-17692.

[42] G. Kresse, J. Furthmüller, *Phys. Rev. B* **1996**, *54*, 11169-11186.

[43] J. P. Perdew, K. Burke, M. Ernzerhof, *Phys. Rev. Lett.* **1996**, *77*, 3865-3868.

[44] L. Vega, F. Viñes, *J. Comput. Chem.* **2020**, *41*, 2598-2603.

[45] S. Grimme, S. Ehrlich, L. Goerigk, *J. Comput. Chem.* **2011**, *32*, 1456-1465.

[46] P. E. Blöchl, *Phys. Rev. B* **1994**, *50*, 17953-17979.

[47] H. J. Monkhorst, J. D. Pack, *Phys. Rev. B* **1976**, *13*, 5188-5192.

[48] G. Henkelman, H. Jónsson, *J. Chem. Phys.* **2000**, *113*, 9978-9985.

[49] G. Henkelman, B. P. Uberuaga, H. Jónsson, *J. Chem. Phys.* **2000**, *113*, 9901-9904.

[50] G. Henkelman, H. Jónsson, *J. Chem. Phys.* **1999**, *111*, 7010-7022.

[51] D. A. McQuarrie, *Statistical Mechanics*, 1 ed., University Science Books, Sausalito, CA, **2000**.

[52] P. Deshlahra, E. Iglesia, *J. Phys. Chem. C* **2014**, *118*, 26115-26129.

[53] P. Deshlahra, E. Iglesia, *J. Phys. Chem. C* **2016**, *120*, 16741-16760.

[54] L. H. Sprowl, C. T. Campbell, L. Árnadóttir, *J. Phys. Chem. C* **2016**, *120*, 9719-9731.

[55] T. J. Boerner, S. Deems, T. R. Furlani, S. L. Knuth, J. Towns, ACM, **2023**.

Entry for the Table of Contents

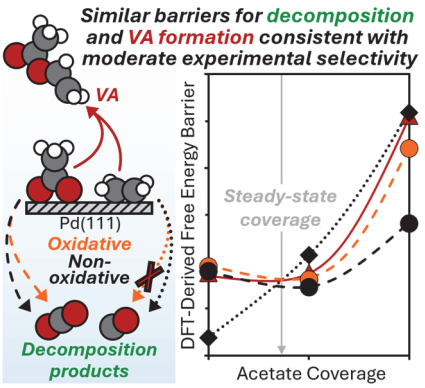

Understanding atomistic origins of catalytic activity and selectivity is crucial for developing improved catalysts for sustainable chemical processes. We present a detailed mechanistic framework derived from theory and experiment to describe complex trends in rate and selectivity for vinyl acetate synthesis on Pd nanoparticle catalysts under high acetate coverage.